

1
2
3
4
5
6
7
8
9
10
11
12
13
14
15
16
17
18
19
20
21
22
23
24
25
26
27
28
29
30
31
32
33
34
35
36
37
38
39
40
41
42
43

EUSO-TA – first results from a ground-based EUSO telescope

G. Abdellaoui^{ah}, S. Abe^{fq}, J.H. Adams Jr.^{pd}, A. Ahriche^{ae}, D. Allard^{cc},
L. Allen^{pb}, G. Alonso^{md}, L. Anchordoqui^{pf}, A. Anzalone^{eh,ed}, Y. Arai^{fs},
K. Asano^{fe}, R. Attallah^{ac}, H. Attoui^{aa}, M. Ave Pernas^{mc}, S. Bacholle^{pc},
M. Bakiri^{aa}, P. Baragatti^{en}, P. Barrillon^{ca}, S. Bartocci^{en}, J. Bayer^{dd},
B. Beldjilali^{ah}, T. Belenguer^{mb}, N. Belkhalifa^{aa}, R. Bellotti^{ea,eb}, A. Belov^{kc},
K. Belov^{pe}, J.W. Belz^{pi}, K. Benmessai^{aa}, M. Bertaina^{ek,el}, P.L. Biermann^{db},
S. Biktemerova^{ka}, F. Bisconti^{db}, N. Blanc^{oa}, J. Błęcki^{ic}, S. Blin-Bondil^{cb},
P. Bobik^{la}, M. Bogomilov^{ba}, E. Bozzo^{ob}, A. Bruno^{eb}, K.S. Caballero^{he},
F. Cafagna^{ea}, D. Campana^{ef}, J-N. Capdevielle^{cc}, F. Capel^{na}, A. Caramete^{ja},
L. Caramete^{ja}, P. Carlson^{na}, R. Caruso^{ec,ed}, M. Casolino^{ft,ei}, C. Cassardo^{ek,el},
A. Castellina^{ek,em}, O. Catalano^{eh,ed}, A. Cellino^{ek,em}, M. Chikawa^{fc},
G. Chiritoi^{ja}, M.J. Christl^{pg}, V. Connaughton^{pd}, L. Conti^{en}, G. Cordero^{ha},
G. Cotto^{ek,el}, H.J. Crawford^{pa}, R. Cremonini^{el}, S. Csorna^{ph}, A. Cummings^{pc},
S. Dagoret-Campagne^{ca}, C. De Donato^{ei}, C. de la Taille^{cb}, C. De Santis^{ei}, L. del
Peral^{mc}, M. Di Martino^{em}, A. Diaz Damian^{cd}, T. Djemil^{ac}, I. Dutan^{ja},
A. Ebersoldt^{db}, T. Ebisuzaki^{ft}, R. Engel^{db}, J. Eser^{pc}, F. Fenu^{ek,el},
S. Fernández-González^{ma}, J. Fernández-Soriano^{mc}, S. Ferrarese^{ek,el},
M. Flamini^{en}, C. Fornaro^{en}, M. Fouka^{ab}, A. Franceschi^{ee}, S. Franchini^{md},
C. Fuglesang^{na}, T. Fujii^{fe}, J. Fujimoto^{fs}, M. Fukushima^{fe}, P. Galeotti^{ek,el},
E. García-Ortega^{ma}, G. Garipov^{kc}, E. Gascón^{ma}, J. Genci^{lb}, G. Girauda^{ek},
C. González Alvarado^{mb}, P. Gorodetzky^{cc}, R. Greg^{pc}, F. Guarino^{ef,eg},
A. Guzmán^{dd}, Y. Hachisu^{ft}, M. Haiduc^{ja}, B. Harlov^{kb}, A. Haungs^{db},
J. Hernández Carretero^{mc}, W. Hidber Cruz^{ha}, D. Ikeda^{fe}, N. Inoue^{fn}, S. Inoue^{ft},
F. Isgro^{ef,en}, Y. Itow^{fk}, T. Jammer^{dc}, S. Jeong^{gc}, E. Joven^{me}, E.G. Judd^{pa},
A. Jung^{cc}, J. Jochum^{dc}, F. Kajino^{ff}, T. Kajino^{fi}, S. Kalli^{af}, I. Kaneko^{ft},
Y. Karadzhov^{ba}, J. Karczmarczyk^{ib}, K. Katahira^{ft}, K. Kawai^{ft}, Y. Kawasaki^{ft},
A. Kedadra^{aa}, H. Khales^{aa}, B.A. Khrenov^{kc}, Jeong-Sook Kim^{ga},
Soon-Wook Kim^{ga}, M. Kleifges^{db}, P.A. Klimov^{kc}, D. Kolev^{ba}, H. Krantz^{pc},
I. Kreykenbohm^{da}, K. Kudela^{la}, Y. Kurihara^{fs}, A. Kusenko^{fr,pe}, E. Kuznetsov^{pd},
A. La Barbera^{eh,ed}, C. Lachaud^{cc}, H. Lahmar^{aa}, F. Lakhdari^{ag}, O. Larsson^{na},
J. Lee^{gc}, J. Licandro^{me}, L. López Campano^{ma}, M.C. MacCarone^{eh,ed},
S. Mackovjak^{ob}, M. Mahdi^{aa}, D. Maravilla^{ha}, L. Marcelli^{ei}, J.L. Marcos^{ma},
A. Marini^{ee}, W. Marszał^{ib}, K. Martens^{fr}, Y. Martín^{me}, O. Martínez^{hc},
M. Martucci^{ee}, G. Masciantonio^{ei}, K. Mase^{fa}, M. Mustafa^{pd}, R. Matev^{ba},
J.N. Matthews^{pi}, N. Mebarki^{ad}, G. Medina-Tanco^{ha}, M.A. Mendoza^{hd},
A. Menshikov^{db}, A. Merino^{ma}, J. Meseguer^{md}, S.S. Meyer^{pb}, J. Mimouni^{ad},
H. Miyamoto^{ek,el}, Y. Mizumoto^{fi}, A. Monaco^{ea,eb}, J.A. Morales de los Ríos^{mc},
S. Nagataki^{ft}, S. Naitamor^{ab}, T. Napolitano^{ee}, R. Nava^{ha}, A. Neronov^{ob},
K. Nomoto^{fr}, T. Nonaka^{fe}, T. Ogawa^{ft}, S. Ogio^{fl}, H. Ohmori^{ft}, A.V. Olinto^{pb},
P. Orleński^{ic}, G. Osteria^{ef}, A. Pagliaro^{eh,ed}, W. Painter^{db}, M.I. Panasyuk^{kc},
B. Panico^{ef}, E. Parizot^{cc}, I.H. Park^{gc}, B. Pastircak^{la}, T. Patzak^{cc}, T. Paul^{pf},

44 I. Pérez-Grande^{md}, F. Perfetto^{ef,eg}, T. Peter^{oc}, P. Picozza^{ei,ej,ft}, S. Pindado^{md},
 45 L.W. Piotrowski^{ft}, S. Piraino^{dd}, L. Placidi^{en}, Z. Plebaniak^{ib}, S. Pliego^{ha},
 46 A. Pollini^{oa}, Z. Polonski^{pc}, E.M. Popescu^{ja}, P. Prat^{cc}, G. Prévôt^{cc}, H. Prieto^{mc},
 47 G. Puehlhofer^{dd}, M. Putis^{la}, J. Rabanal^{ca}, A.A. Radu^{ja}, M. Reyes^{me},
 48 M. Rezazadeh^{pb}, M. Ricci^{ee}, M.D. Rodríguez Frías^{mc}, F. Ronga^{ee}, G. Roudil^{cd},
 49 I. Rusinov^{ba}, M. Rybczyński^{ia}, M.D. Sabau^{mb}, G. Sáez Cano^{mc}, H. Sagawa^{fe},
 50 Z. Sahnoune^{ab}, A. Saito^{fg}, N. Sakaki^{fe}, H. Salazar^{hc}, J.C. Sanchez Balanzar^{ha},
 51 J.L. Sánchez^{ma}, A. Santangelo^{dd}, A. Sanz-Andrés^{md}, M. Sanz Palomino^{mb},
 52 O. Saprykin^{kb}, F. Sarazin^{pc}, M. Sato^{fo}, T. Schanz^{dd}, H. Schieler^{db}, V. Scotti^{ef,eg},
 53 S. Selmane^{cc}, D. Semikoz^{cc}, M. Serra^{me}, S. Sharakin^{kc}, H.M. Shimizu^{jj},
 54 H.S. Shin^{fe}, K. Shinozaki^{la}, T. Shirahama^{fn}, P. Sokolsky^{pi}, B. Spataro^{ee},
 55 I. Stan^{ja}, T. Sugiyama^{jj}, D. Supanitsky^{ha}, M. Suzuki^{fm}, B. Szabelska^{ib},
 56 J. Szabelski^{ib}, N. Tajima^{ft}, T. Tajima^{ft}, Y. Takahashi^{fo}, H. Takami^{fs},
 57 M. Takeda^{fe}, Y. Takizawa^{ft}, M.C. Talai^{ac}, Y. Tameda^{pj}, C. Tenzer^{dd},
 58 S.B. Thomas^{pi}, G.B. Thomson^{pi}, O. Tibolla^{hf}, L. Tkachev^{ka}, H. Tokuno^{fp},
 59 T. Tomida^{fh}, N. Tone^{ft}, S. Toscano^{ob}, M. Traïche^{aa}, R. Tsenov^{ba},
 60 Y. Tsunesada^{fl}, K. Tsuno^{ft}, J. Tubbs^{pd}, S. Turriziani^{ft}, Y. Uchihori^{fb},
 61 O. Vaduvescu^{me}, J.F. Valdés-Galicia^{ha}, P. Vallania^{ek,em}, G. Vankova^{ba},
 62 C. Vigorito^{ek,el}, L. Villaseñor^{hb}, B. Vlcek^{mc}, P. von Ballmoos^{cd}, M. Vrabel^{lb},
 63 S. Wada^{ft}, J. Watanabe^{fi}, J. Watts Jr.^{pd}, M. Weber^{db}, R. Weigand Muñoz^{ma},
 64 A. Weindl^{db}, L. Wiencke^{pc}, M. Wille^{da}, J. Wilms^{da}, Z. Włodarczyk^{ia},
 65 T. Yamamoto^{ff}, J. Yang^{gb}, H. Yano^{fm}, I.V. Yashin^{kc}, D. Yonetoku^{fd},
 66 S. Yoshida^{fa}, R. Young^{pg}, I.S Zgura^{ja}, M.Yu. Zotov^{kc}, A. Zuccaro Marchi^{ft aa}

67 Centre for Development of Advanced Technologies (CDTA), Algiers, Algeria
 68 ^{ab} Dep. Astronomy, Centre Res. Astronomy, Astrophysics and Geophysics (CRAAG),
 69 Algiers, Algeria
 70 ^{ac} LPR at Dept. of Physics, Faculty of Sciences, University Badji Mokhtar, Annaba,
 71 Algeria
 72 ^{ad} Lab. of Math. and Sub-Atomic Phys. (LPMPS), Univ. Constantine I, Constantine,
 73 Algeria
 74 ^{ae} Laboratory of Theoretical Physics LPT, University of Jijel, Jijel, Algeria
 75 ^{af} Department of Physics, Faculty of Sciences, University of M'sila, M'sila, Algeria
 76 ^{ag} Research Unit on Optics and Photonics, UROP-CDTA, Sétif, Algeria
 77 ^{ah} Telecom Lab., Faculty of Technology, University Abou Bekr Belkaid, Tlemcen, Algeria
 78 ^{ba} St. Kliment Ohridski University of Sofia, Bulgaria
 79 ^{ca} LAL, Univ Paris-Sud, CNRS/IN2P3, Orsay, France
 80 ^{cb} Omega, Ecole Polytechnique, CNRS/IN2P3, Palaiseau, France
 81 ^{cc} APC, Univ Paris Diderot, CNRS/IN2P3, CEA/Irfu, Obs de Paris, Sorbonne Paris
 82 Cité, France
 83 ^{cd} IRAP, Université de Toulouse, CNRS, Toulouse, France
 84 ^{da} ECAP, University of Erlangen-Nuremberg, Germany
 85 ^{db} Karlsruhe Institute of Technology (KIT), Germany
 86 ^{dc} Experimental Physics Institute, Kepler Center, University of Tübingen, Germany
 87 ^{dd} Institute for Astronomy and Astrophysics, Kepler Center, University of Tübingen,

88 Germany

89 *ea* Istituto Nazionale di Fisica Nucleare - Sezione di Bari, Italy

90 *eb* Università' degli Studi di Bari Aldo Moro and INFN - Sezione di Bari, Italy

91 *ec* Dipartimento di Fisica e Astronomia - Università' di Catania, Italy

92 *ed* Istituto Nazionale di Fisica Nucleare - Sezione di Catania, Italy

93 *ee* Istituto Nazionale di Fisica Nucleare - Laboratori Nazionali di Frascati, Italy

94 *ef* Istituto Nazionale di Fisica Nucleare - Sezione di Napoli, Italy

95 *eg* Università' di Napoli Federico II - Dipartimento di Scienze Fisiche, Italy

96 *eh* INAF - Istituto di Astrofisica Spaziale e Fisica Cosmica di Palermo, Italy

97 *ei* Istituto Nazionale di Fisica Nucleare - Sezione di Roma Tor Vergata, Italy

98 *ej* Università' di Roma Tor Vergata - Dipartimento di Fisica, Roma, Italy

99 *ek* Istituto Nazionale di Fisica Nucleare - Sezione di Torino, Italy

100 *el* Dipartimento di Fisica, Università' di Torino, Italy

101 *em* Osservatorio Astrofisico di Torino, Istituto Nazionale di Astrofisica, Italy

102 *en* UTIU, Dipartimento di Ingegneria, Rome, Italy

103 *eo* DIETI, Università' degli Studi di Napoli Federico II, Napoli, Italy

104 *fa* Chiba University, Chiba, Japan

105 *fb* National Institute of Radiological Sciences, Chiba, Japan

106 *fc* Kinki University, Higashi-Osaka, Japan

107 *fd* Kanazawa University, Kanazawa, Japan

108 *fe* Institute for Cosmic Ray Research, University of Tokyo, Kashiwa, Japan

109 *ff* Konan University, Kobe, Japan

110 *fg* Kyoto University, Kyoto, Japan

111 *fh* Shinshu University, Nagano, Japan

112 *fi* National Astronomical Observatory, Mitaka, Japan

113 *fj* Nagoya University, Nagoya, Japan

114 *fk* Institute for Space-Earth Environmental Research, Nagoya University, Nagoya, Japan

115 *fl* Graduate School of Science, Osaka City University, Japan

116 *fm* Institute of Space and Astronautical Science/JAXA, Sagami-hara, Japan

117 *fn* Saitama University, Saitama, Japan

118 *fo* Hokkaido University, Sapporo, Japan

119 *fp* Interactive Research Center of Science, Tokyo Institute of Technology, Tokyo, Japan

120 *fq* Nihon University Chiyoda, Tokyo, Japan

121 *fr* University of Tokyo, Tokyo, Japan

122 *fs* High Energy Accelerator Research Organization (KEK), Tsukuba, Japan

123 *ft* RIKEN, Wako, Japan

124 *ga* Korea Astronomy and Space Science Institute (KASI), Daejeon, Republic of Korea

125 *gb* Ewha Womans University, Seoul, Republic of Korea

126 *gc* Sungkyunkwan University, Seoul, Republic of Korea

127 *ha* Universidad Nacional Autónoma de México (UNAM), Mexico

128 *hb* Universidad Michoacana de San Nicolas de Hidalgo (UMSNH), Morelia, Mexico

129 *hc* Benemérita Universidad Autónoma de Puebla (BUAP), Mexico

130 *hd* Centro de Desarrollo Aeroespacial - Instituto Politécnico Nacional (CDA-IPN), Mexico

131 *he* Universidad Autónoma de Chiapas (UNACH), Chiapas, Mexico

132 *hf* Centro Mesoamericano de Física Teórica (MCTP), Mexico

133 *ia* Jan Kochanowski University, Institute of Physics, Kielce, Poland
 134 *ib* National Centre for Nuclear Research, Lodz, Poland
 135 *ic* Space Research Centre of the Polish Academy of Sciences (CBK), Warsaw, Poland
 136 *ja* Institute of Space Science ISS, Magurele, Romania
 137 *ka* Joint Institute for Nuclear Research, Dubna, Russia
 138 *kb* Central Research Institute of Machine Building, TsNIIMash, Korolev, Russia
 139 *kc* Skobeltsyn Institute of Nuclear Physics, Lomonosov Moscow State University, Russia
 140 *la* Institute of Experimental Physics, Kosice, Slovakia
 141 *lb* Technical University Kosice (TUKE), Kosice, Slovakia
 142 *ma* Universidad de León (ULE), León, Spain
 143 *mb* Instituto Nacional de Técnica Aeroespacial (INTA), Madrid, Spain
 144 *mc* Universidad de Alcalá (UAH), Madrid, Spain
 145 *md* Universidad Politécnica de madrid (UPM), Madrid, Spain
 146 *me* Instituto de Astrofísica de Canarias (IAC), Tenerife, Spain
 147 *na* KTH Royal Institute of Technology, Stockholm, Sweden
 148 *oa* Swiss Center for Electronics and Microtechnology (CSEM), Neuchâtel, Switzerland
 149 *ob* ISDC Data Centre for Astrophysics, Versoix, Switzerland
 150 *oc* Institute for Atmospheric and Climate Science, ETH Zürich, Switzerland
 151 *pa* Space Science Laboratory, University of California, Berkeley, USA
 152 *pb* University of Chicago, USA
 153 *pc* Colorado School of Mines, Golden, USA
 154 *pd* University of Alabama in Huntsville, Huntsville, USA
 155 *pe* NASA Jet Propulsion Laboratory, Pasadena, USA
 156 *pf* Lehman College, City University of New York (CUNY), USA
 157 *pg* NASA - Marshall Space Flight Center, USA
 158 *ph* Vanderbilt University, Nashville, USA
 159 *pi* University of Utah, Salt Lake City, USA
 160 *pj* Department of Engineering Science, Faculty of Engineering, Osaka
 161 Electro-Communication University, Neyagawa-shi, Osaka, Japan
 162

163 **Abstract**

164 EUSO-TA is a ground-based telescope, installed at the Telescope Ar-
 165 ray (TA) site in Black Rock Mesa, Utah, USA. This is the first detector to
 166 successfully use a Fresnel lens based optical system and multi-anode photo-
 167 multipliers (64 channels per tube, 2304 channels encompassing a $10.6^\circ \times 10.6^\circ$
 168 field of view) for detection of Ultra High Energy Cosmic Rays (UHECR). The
 169 telescope is located in front of one of the fluorescence detectors of the TA
 170 experiment. Since its installation in 2013, the detector has observed several
 171 ultra-high energy cosmic ray events and, in addition, meteors. The limiting

172 magnitude of 5.5 on summed frames (~ 3 ms) has been established. Measure-
173 ments of the UV night sky emission in different conditions and moon phases
174 and positions have been completed. The performed observations serve as a
175 proof of concept for the future application of this detector technology.

176 1. Introduction

177 JEM-EUSO is a proposed space-borne mission concept for the detec-
178 tion of cosmic rays of the highest energies [1]. It is designed to observe the
179 ultraviolet (UV) fluorescence light from Extended Air Showers (EAS) gen-
180 erated by cosmic rays in the atmosphere with a Fresnel lens based optical
181 system and a super-fast single photon counting camera. Compared to ex-
182 isting ground-based experiments, JEM-EUSO would be able to observe a
183 much larger volume of the atmosphere, significantly increasing the number
184 of detected events at the highest energies and thus the available data for the
185 localisation of their sources in the Universe.

186 The first attempt to use Fresnel lenses to observe EAS was made in late
187 sixties near Ithaca, USA, resulting in measurements of a Xenon flasher cali-
188 bration light source [2]. The first observations in the framework of the EUSO
189 concept have been performed with the ground-based experiment EUSO-TA,
190 which is the main focus of this paper. The flight of EUSO-BALLOON, with
191 similar design, followed in 2014 [3] and successfully observed laser-simulated
192 EAS, LED flashes and the night-time UV emission of Earth. In 2017 a super
193 pressure balloon with upgraded electronics – EUSO-SPB – has flown with
194 a pioneering aim of observing UV light from EAS looking down on the at-
195 mosphere. Currently, another mission is in the final stage of preparation
196 – Mini-EUSO – designed to be hosted inside the International Space Sta-
197 tion, observing the atmosphere through a UV-transparent window [4]. Mini-
198 EUSO will be sensitive to EAS with primary energies above 10^{21} eV, meteors,
199 strange quark matter and atmospheric events such as Transient Luminous
200 Events (TLEs). It will also produce a detailed UV map of the night-time
201 Earth. It will be followed by K-EUSO – a mission led by Russian Space
202 Agency, placing an UHECR observatory on board the Russian Segment of
203 the ISS [5, 6].

204 EUSO-TA is a ground-based telescope located at Black Rock Mesa, Utah,
205 USA at the site of one of the fluorescence detectors of the Telescope Array
206 (TA) experiment [7] (fig. 1). From there it observes, simultaneously with



Figure 1: EUSO-TA (front right), EUSO-SPB (front middle, temporarily installed on-site before its flight) and Telescope Array Fluorescence Detector (TAFD, back) (photography by M. Mustafa)

207 TA, both artificial calibration light and cosmic ray events, allowing for tests
 208 of the EUSO technology, calibration of the detector and reduction of the
 209 systematic uncertainties of the measurements. The location and pointing
 210 direction allows for observation of TA's Central Laser Facility (CLF) and
 211 Electron Light Source (ELS) (fig. 2).

212 **2. EUSO-TA instrument**

213 The 1 m^2 EUSO-TA Fresnel lenses (0.92 m^2 active area) are fabricated
 214 from UV transmitting polymethyl-methacrylate (PMMA). The baseline de-
 215 sign of the optics is shown in fig. 3 with ray tracing for incident angles of
 216 0° , 2° , 4° and 6° with respect to the optical axis, covering a 10.6° (in elevation)
 217 $\times 10.6^\circ$ (in azimuth) field of view.

218 The lenses (fig. 4, left) focus light onto the $17.3 \text{ cm} \times 17.3 \text{ cm}$ Photo De-
 219 tector Module (PDM), composed of 36 Multi-Anode Photomultiplier Tubes
 220 (MAPMTs) [8] each containing 64 anodes, for a total of 2304 pixels (fig. 4,
 221 right), covered by BG3 filters. Four MAPMTs form an EC-Unit, each with a
 222 dedicated Cockroft-Walton based High Voltage Power Supply. The operating

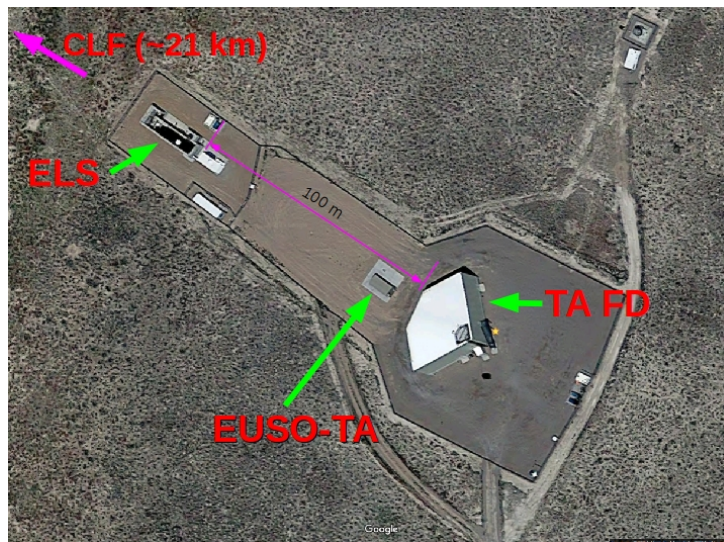


Figure 2: The position of EUSO-TA on the Telescope Array Fluorescence Detector site in Black Rock Mesa, Utah, USA. The EUSO-TA container is placed directly in front of the TAFD. In its line of sight are the Electron Light Source and the Central Laser Facility instruments of TA. Original photography taken from Google Maps.

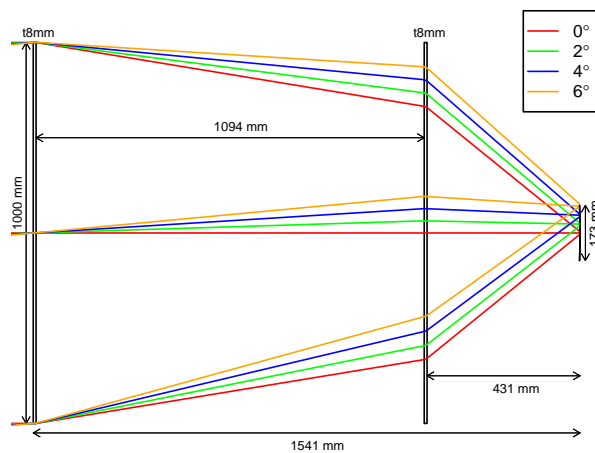


Figure 3: The design of the EUSO-TA optics. The ray tracing is shown for different incident angles of 0° , 2° , 4° and 6° , respectively.

223 voltage of the MAPMTs is 1000 V, and is automatically reduced on scale of
224 microseconds in the case of high incident photon flux.

225 Each MAPMT is read out by one of the SPACIROC1 ASICs, which are
226 distributed over 6 EC-ASIC boards [9]. The single pulse resolution of the
227 ASICs is ~ 30 ns. This implies a saturation at about 28 counts (photoelec-
228 trons) for each frame – one Gate Time Unit (GTU) – of $2.3 \mu\text{s}$. The frame
229 is preceded by 200 ns of dead time. This dead time has been reduced to 50
230 ns in the next generation ASIC – SPACIROC3 – which has a single pulse
231 resolution of ~ 5 ns and thus, being able to count more photons in given
232 period of time, a higher signal to noise ratio. SPACIROC3 has already been
233 used in both EUSO-SPB and Mini-EUSO. EUSO-TA will be upgraded to
234 SPACIROC3 during 2018.

235 The digitised counts from 6 EC-ASIC boards are read into a ring buffer
236 on the PDM board. This buffer can accommodate 128 GTUs and is read
237 out following an external or internal trigger. One of the main tasks of the
238 PDM board is to perform high-speed, first-level triggering (L1) and then for-
239 ward the selected packet of 128 frames to the Cluster Control Board (CCB).
240 EUSO-TA is usually operated with an external trigger from TAFD. Although
241 implemented in EUSO-TA, the L1 trigger is not optimised for the ground-
242 based configuration due to geometrical constraints (see sec. 4.4).

243 The CCB, which contains a second-level trigger board [10], CPU, Clock
244 board (CLKB), GPS, house keeping and low voltage power supply [11] forms
245 the Data Processor (DP) unit [12]. The exchange of information is made
246 with encapsulated packets. The amount of information contained in a packet
247 increases with the level of processing, the final packet stored by the CPU on a
248 hard disk contains counts from ASICs, additional information from the PDM
249 board, CCB, CLKB and GPS data [13]. The whole data readout scheme is
250 summarised in fig. 5.

251 The focal surface and lenses are mounted on a stand with an adjustable
252 elevation angle between 0° and 30° . The stand is installed in a container
253 placed in front of the Telescope Array Fluorescence Detector (TAFD) tele-
254 scope, but below its field of view. Apart from protecting the detector and
255 additional electronics from weather conditions, the walls of the container
256 reduce the stray light entering the instrument.

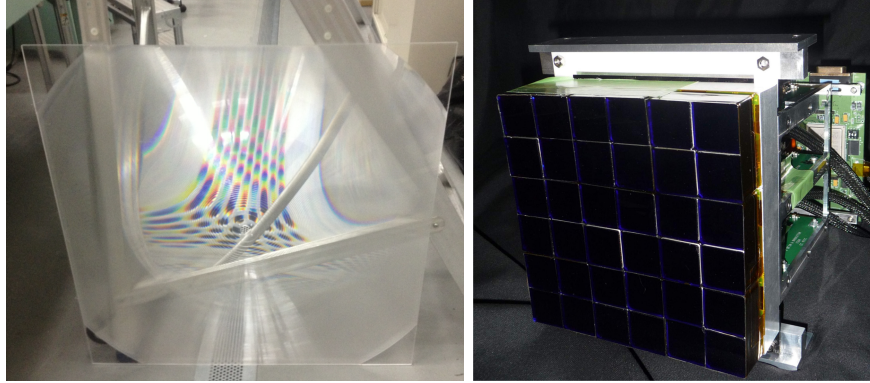


Figure 4: Left: front 1 m² lens of EUSO-TA; Right: the PDM array of side 17.3 cm, composed of 36 MAPMTs, 64 channels each. Behind it 6 ASIC boards are mounted on the PDM frame connected to the PDM board.

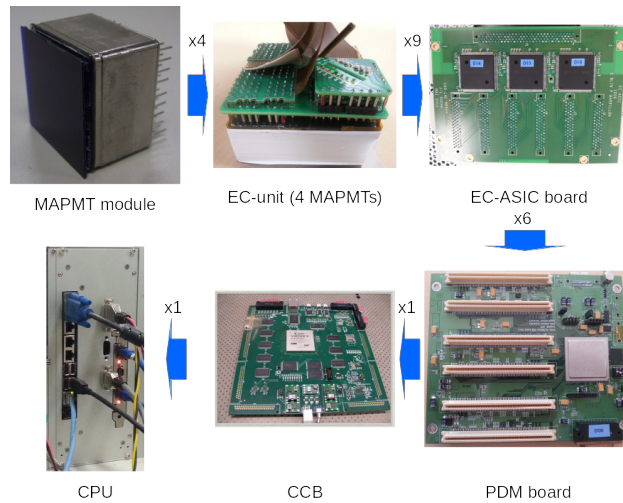


Figure 5: Scheme of the signal flow in the EUSO-TA experiment. The labels over arrows denote signal from how many subsystems of the previous level is included in the subsystem of the next level.

257 **3. EUSO-TA observation campaigns**

258 The EUSO-TA lenses and mechanical structure were installed in TAFD
259 site in Black Rock Mesa, Utah, USA in March 2013. After the installa-
260 tion, initial tests of the optics and mechanics were performed using a single
261 MAPMT with a temporary readout scheme.

262 Prior to the commissioning of the complete EUSO-TA instrument, its
263 lenses and mechanics were used in the one-pixel UHECR detector “FAST”
264 tests in April and June 2014 [14]. The EUSO-TA PDM and readout system
265 were installed in February-March 2015. Since then, 5 observational cam-
266 paigns with EUSO-TA have been performed, 4 in 2015 and 1 in 2016. More
267 than 136 hours of observation have been acquired using the TAFD exter-
268 nal trigger, thus allowing for coincident detection of UHECR events in the
269 overlapping field of view of the two instruments.

270 More than 21 hours of data were dedicated to observations using different
271 triggers, usually for synchronising with laser shots, LED flashes and tests of
272 the internal L1 trigger of EUSO experiments. The L1 trigger is tuned to fu-
273 ture in-orbit EUSO observations, for which the timescale of an EAS crossing
274 the field of view is much longer, and thus it is not optimal for ground-based
275 observations with the same time resolution. For this reason, the external trig-
276 ger from TAFD was also implemented in EUSO-TA. However, the controlled
277 signals produced by the laser allowed us to analyse the efficiency of the L1
278 trigger and fine-tune it for the application in EUSO-SPB and Mini-EUSO.

279 In October 2016, the EUSO-SPB telescope was transported to the EUSO-
280 TA site with a specially modified trailer for ground-based tests and calibra-
281 tion. This allowed for simultaneous observations with the two detectors shar-
282 ing the same design, the main difference being the upgraded SPACIROC3
283 ASICs in EUSO-SPB.

284 **4. Results**

285 *4.1. Sky background*

286 The average sky emission¹ on the EUSO-TA focal surface for a typical
287 dark, cloudless night period (16th of May, 2015, from 9:13 to 9:29 UTC) was
288 1.43 counts per 2.3 μ s (fig. 6, left). The background histogram consists of

¹Here “sky emission” is understood to be light registered by the detector excluding distinguishable light sources.

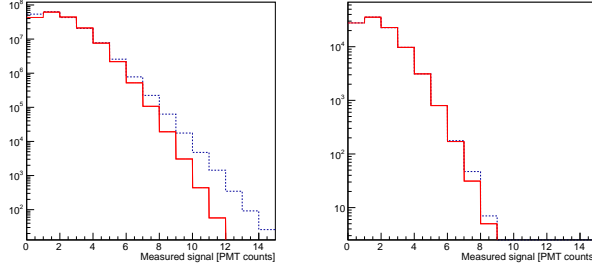


Figure 6: Left: histogram of counts in all working pixels of the focal surface from 100000 frames (dashed) and a fitted Poisson distribution (solid), for sky background observations on the night of 16th of May, 2015. Right: similar histogram consisting of counts in a single pixel.

289 measurements of pixels with varying efficiencies, and hence varying count
 290 distributions. In this way, the overall distribution deviates from Poissonian
 291 for high values. The number of counts on a single pixel, which is sensitive
 292 to single photons, is well described by the Poisson distribution, as can be
 293 seen on fig. 6, right. This sample pixel has an average number of counts per
 294 frame on 100000 frames equal to 1.28. In the simplest case, the counts in
 295 this pixel would have to exceed 3σ threshold of about 5.8 counts to detect a
 296 signal. However, the phenomena of observational interest extend over many
 297 pixels, lowering this requirement when using more sophisticated detection
 298 algorithms.

299 The baseline background depends on a number of factors such as the
 300 time of the night, moon phase, time of the year and the presence of clouds
 301 and aerosols. In fig. 7 the variation of the average number of counts on the
 302 whole focal surface is shown during one slightly cloudy night (16th of May,
 303 2015), with a baseline background level higher than 2 counts. The smooth
 304 variation is interrupted by clouds passing through the field of view, as shown
 305 in fig. 8. In the case of observations of the sky from the ground, clouds
 306 can both decrease and increase the background. The decrease can come
 307 from the eclipsing of the nightglow, zodiacal light, milky way and single
 308 stars. The increase can come from the reflection of the artificial ground-
 309 based lights or from the scattering of the moonlight in moonlit nights. In the
 310 case shown, clouds decrease the number of counts, as they block radiation
 311 from the nightglow and astronomical objects.

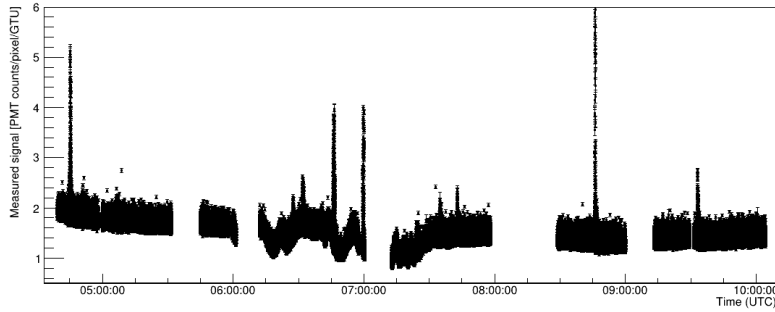


Figure 7: Average signal on the whole focal surface as a function of time for the night of the 16th of May, 2015. The changes visible on timescales of dozens of minutes are as a result of clouds and stars passing through the field of view, whilst more rapid changes are due to the movement of airplanes. The gaps in data correspond to breaks in observations. The X-axis spans roughly from 22:00 to 4:00 of local “Mountain Time” (UTC-06:00).

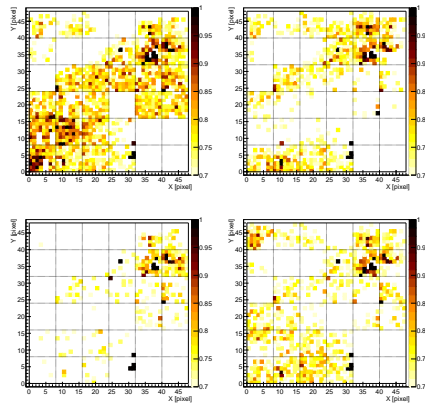


Figure 8: Examples of clouds (dark areas) passing through the focal surface. The four pictures show averages of 1280 frames separated by a few minutes. The colour scale denotes the brightness of each pixel in arbitrary units after flat fielding. This and all the following figures of this kind show the view of the observer standing behind the instrument and looking at the same part of the sky.

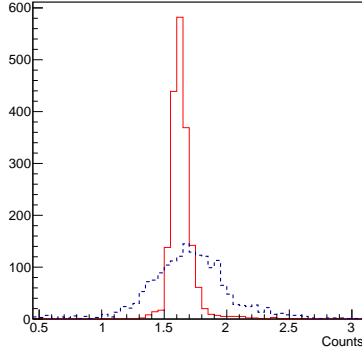


Figure 9: Histogram of sky background pixel counts on an average of 12800 frames before (dashed) and after (solid) flat fielding.

312 *4.1.1. Flat fielding*

313 It is a common practice in scientific imaging to equalise pixel sensitivities
 314 during data processing. This is especially important for a photomultiplier
 315 based photon counter, for which pixels can vary significantly in their efficien-
 316 cies. For this purpose, flat fielding is often employed. This involves illumi-
 317 nating the telescope with a uniform, Lambertian light source. To achieve this
 318 for EUSO-TA, a large reflective flat screen illuminated by a diffused LED was
 319 used. The 2.44 m \times 2.44 m flat screen was covered with Tyvek and placed
 320 6.5 m in front of the EUSO-TA front lens. The LED was placed in the centre
 321 of the front lens, emitting light of wavelength 375 nm through a 3.2° neutral
 322 density filter. The non-uniformity of the detector illumination coming from
 323 this setup is small compared to the uncertainties from other sources, mainly
 324 due to the fact that the detector was focused at infinity [15].

325 The flat fielding drastically reduces the width of the pixel counts distri-
 326 bution. On a sample averaged sky frame generated from 12800 GTUs², the
 327 width of the distribution before flat fielding was 24.6%, while after it dropped
 328 to 9.3% (fig. 9). It is important to note that the photographed sky is not
 329 completely uniform (due to stars and diffuse sky light sources), so quoted
 330 numbers are just a relative estimation of the improvement.

²Usually we are using multiples of 128 for frame stacking, since one full packet of data continuous in time consists of 128 frames.

331 *4.2. Star observations*

332 Stars can be used as point sources to analyse the sensitivity, the extent of
333 the field of view and the point spread function (PSF) of the detector. EUSO-
334 TA can observe stars up to $M_B \simeq 5.5$ (catalogue magnitude in Johnson B
335 filter [16]) on sums of 1280 frames (about 3.2 ms observation time). This
336 limiting magnitude is a very approximate measure of EUSO-TA sensitivity,
337 since it depends largely on the spectral properties of the star in question and
338 atmospheric conditions at the time of observation (the EUSO-TA spectral
339 window is far from standard Johnson filters). Moreover, the small number of
340 sufficiently bright stars in the field of view do not allow for a precise estimate.

341 Frame stacking can be used to achieve a better signal to noise ratio,
342 thanks to negligible movement of the stars on the sky for short observation
343 timescales compared to the angular size of a pixel. An example of 1280
344 stacked frames with a few stars clearly visible is shown in fig. 10. The
345 brightest star positions are marked on the image following the Hipparcos
346 catalogue [17].

347 The very wide field of view results in an asymmetric PSF in regions of
348 the focal surface far from the optical axis due to influence of aberrations such
349 as coma or astigmatism. In this way, a complete analysis would be based on
350 fitting the parameters of a PSF model derived from theory and ray-tracing
351 simulations to the images of the stars in different positions on the frame,
352 which is a demanding and difficult task even in detectors with much finer
353 angular resolution [18]. An approach making use of an elliptical Gaussian
354 profile fit gives an asymmetric PSF (fig. 11) with an average FWHM of
355 2.98 ± 0.07 and 2.46 ± 0.04 pixels for the major and minor axes of the ellipse,
356 respectively [19]. This result is well within the requirements for observations
357 of UHECR showers. However, the near-constant asymmetry of the ellipse
358 regardless of the position of the star image on the focal surface suggests a
359 misalignment of the planes of the focal surface and the lenses. This effect
360 likely hides the aforementioned aberrations of the PSF.

361 The small PSF observed for stationary sources such as stars, but also for
362 laser signals, is important for future, space-based observations of UHECR.
363 Current ground-based experiments employ optics with much larger pixel and
364 PSF size, which would result in poor performance for EAS observations at
365 distances of hundreds of kilometres. Auger's fluorescence detectors have
366 hexagonal pixels with side to side distance of 45.6 mm, corresponding to
367 1.5° field of view [20]. Similarly, TAFD pixels are hexagonal in shape with a
368 distance of 60 mm between the parallel side and cover $1.1^\circ \times 1.0^\circ$ patch of

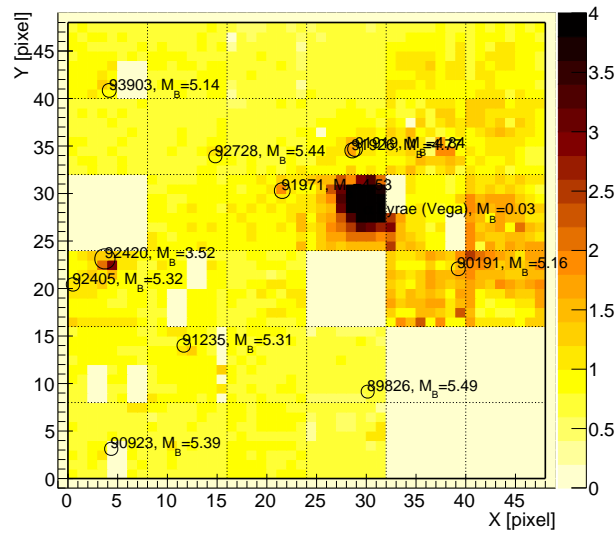


Figure 10: Sum of 1280 frames acquired with EUSO-TA with the position of the brightest stars superimposed, using the Hipparcos catalogue. Each star is labelled with the catalogue number or the star name in case of Vega, followed by the star's magnitude in the Johnson B filter for objects of $M_B \leq 5.5$. The colour scale denotes the brightness of each pixel in arbitrary units after flat fielding. Zero values (light yellow) correspond to non-functioning pixels.

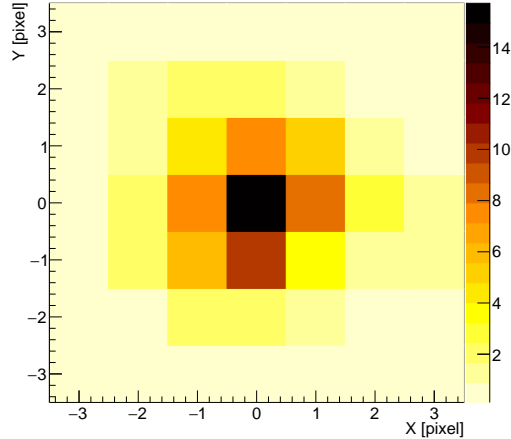


Figure 11: Sum of 12800 frames (about 1 minute) of observations of a typical star for the purpose of PSF estimation. Colours denote the percentage of a signal in the specific bin. This star has Hipparcos catalogue number 100453 with brightness $M_B = 2.9$.

369 the sky [21]. For comparison, with EUSO-TA a distant source image, such
 370 as that from a star, fits within a rectangle of 3×3 pixels, each a square of
 371 0.288 cm side, and angular size of $\sim 0.19^\circ$.

372 The observation of stars allows for astrometry, i.e. determination of the
 373 detector's pointing direction in celestial coordinates. For EUSO-TA this was
 374 also used to compute the field of view, resulting in $10.6^\circ \pm 0.3^\circ$ in both
 375 dimensions. Again, the uncertainty is mostly due to the small number of
 376 bright stars within the range of the detector, which in turn makes a more
 377 sophisticated estimation of the parameters, such as those of a polynomial
 378 description of the optical distortion, difficult.

379 *4.3. Slow phenomena*

380 Whilst EUSO-TA is designed for observations of microsecond-scale events,
 381 it can also monitor phenomena taking place on much longer timescales. The
 382 most common are flashes from airplanes and sunlight reflected by satellites.
 383 Satellite observations can be used as a proof of concept for the plans of space
 384 debris remediation with future, orbital EUSO-like experiments [22].

385 EUSO-TA has also observed meteors, as can be seen in fig. 12. The
 386 magnitudes of three of the observed meteors are shown in tab. 1. Such

Date	Lowest magnitude	Highest magnitude
2015.09.18	1.59 ± 0.20	5.27 ± 0.20
2015.11.12	2.40 ± 0.11	4.06 ± 0.11
2015.11.13	1.91 ± 0.03	3.04 ± 0.05

Table 1: Apparent magnitude of three meteors as observed by EUSO-TA

387 observations are unique due to their microseconds to seconds time resolution.
388 This property can be useful to improve our capability to detect the details of
389 the ablation processes undergone by the meteoroid during its passage through
390 the atmosphere. In other words, EUSO-TA can produce meteor lightcurves
391 of much better time resolution than other detectors usually doing meteor
392 observations. In addition, this is related to a better estimation of the meteor
393 speed and more precise determination of the original heliocentric orbit of the
394 meteoroid if we were to perform multi-detector observations in the future.

395 High time resolution and large field of view is important also for the possi-
396 ble detection of a phenomenon similar in appearance to meteors – strangelets
397 [23]. These nuggets of strange matter are predicted to interact with the
398 atmosphere producing light, however with a different lightcurve than that
399 of meteors due to the fact that they do not fragment or lose mass. After
400 90 cumulative days of observations, EUSO-TA will be able to set limits on
401 strangelets of mass above 5×10^{23} GeV/ c^2 that are more stringent than exist-
402 ing limits [23]. For this task a dedicated autonomous trigger is in preparation,
403 as the external trigger from TAFD is designed to discard constant and slow
404 moving events from the data stream such as airplanes.

405 The faintest meteor observed had an apparent magnitude of $M_B = 2.4 \pm$
406 0.11 , but was still very bright on the frames and easily detectable. If the
407 same detection limit as for stars is assumed – $M_B = 5.5$, then an average
408 detection rate of about 1 meteor per hour of observation is expected, upon
409 the introduction of a dedicated trigger algorithm.

410 A thunderstorm occurred during one of the observation campaigns of
411 EUSO-TA, and the influence of lightning on the focal surface was registered.
412 Due to the relatively slow timescale of lightning development relative to the
413 packet length, without a dedicated trigger it was only possible to catch the
414 rising slope of the phenomenon (fig. 13). The thunderstorm took place

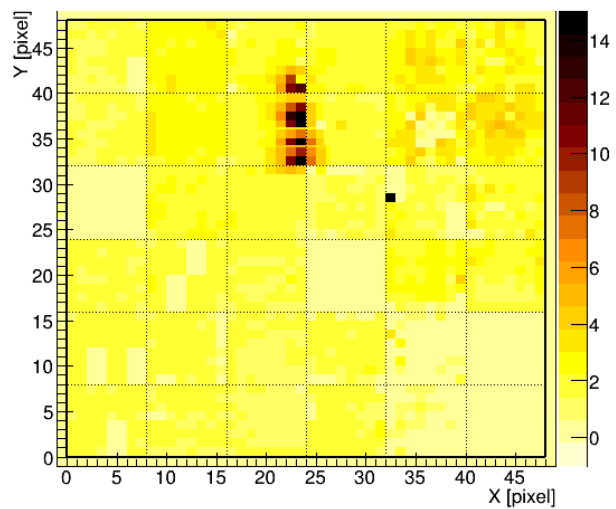


Figure 12: A meteor track detected by EUSO-TA on the night 12th November, 2015. The picture shows the overlap of four averages of 1280 frames (0.9 s elapsed from the start to the end of the observation, 12.8 ms total integration time). The color scale denotes the uncalibrated detector counts. The apparent magnitude of the meteor in collected data varied from $M_B = 2.4$ to $M_B = 4.06$.

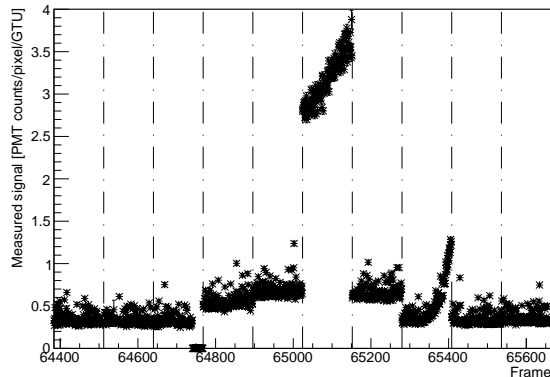


Figure 13: The lightcurve of the average number of counts per $2.3 \mu s$ on the whole PDM during a thunderstorm passing close by. The lightcurve is not continuous. Vertical lines show the transition between packets of data. Each packet is a continuous acquisition encompassing $320 \mu s$, however the time between packets depends on incoming triggers and in this case was of order of dozens of milliseconds.

415 outside of the field of view of the telescope³, thus no distinct features were
 416 visible. In separate tests it has been confirmed that the EUSO-TA electronics
 417 can be influenced by strong radio signals, resulting in rise of counts on the
 418 focal surface. In this way, it is not possible to conclude if the registered
 419 changes in counts are due to scattered light from the storm, or its radio
 420 emission.

421 High time resolution is required for observations of another thunderstorm
 422 related phenomena – TLEs – such as “sprites” and “elves”, occurring high
 423 above the clouds on timescales of dozens of micro- to milliseconds. EUSO-TA
 424 should be able to detect some events of this kind after its planned upgrade
 425 (sec. 5).

426 4.4. Laser observations

427 In order to study the response of EUSO-TA to a known light source
 428 the light coming from TA’s CLF has been used, situated at a distance of
 429 about 21 km from EUSO-TA. The CLF shoots a laser of 355 nm wavelength

³Position of the thunderstorm with respect to the field of view was inspected visually by EUSO-TA shifters on-site.

430 vertically in front of the detectors [24].

431 During standard observations, the CLF is shot every half an hour for 30
432 s at a shooting frequency of 10 Hz. The scattered light of the ~ 3 mJ beam
433 is clearly visible when traversing through the EUSO-TA field of view on 6 to
434 8 frames, depending on the shot and acquisition time synchronisation. The
435 spot length is 6-8 pixels depending on the position on the frame (fig. 14,
436 inset), which is consistent with expectations. The registered light intensity
437 drops as the laser travels up in the field of view, as shown in fig. 15. This
438 is due to the increasing distance of the laser to the detector. The initial fast
439 rise and final drop are due to the track entering and leaving the focal surface,
440 while the intermediate drops are caused by dead spaces between MAPMTs.
441 The brightness spread, defined as a standard deviation of the summed counts
442 from a laser track in the EUSO-TA field of view, as measured by the detector
443 is 5% (fig. 16), comparable with an intrinsic CLF energy spread of 6%.

444 In fig. 17 the width of the CLF track as a function of its vertical position
445 on the frame is shown, measured as a FWHM of a fitted gaussian profile.
446 The width changes from about 3.8 pixels at the edges of the field of view
447 to about 2.8 pixels in the centre of the frame. The last value is consistent
448 with the measured PSF of star images. The dependency of the width on the
449 position on the frame can be explained by the increasing influence of optical
450 aberration with distance from the optical axis.

451 In addition to the CLF measurements, shooting of the Global Light Sys-
452 tem (GLS) [25] laser – a mobile UV laser of the Colorado School of Mines
453 was also performed. The laser can be shot with energies in the range of
454 about 1–86 mJ, with the pointing direction adjustable in two dimensions.
455 The mechanics featured automatic changing of the pointing direction, al-
456 lowing for easy “swipes” through the field of view. In addition the GLS
457 laser produced events whose distance to the detector increased with time,
458 as expected in space-based observation of cosmic rays. Initial results of the
459 direction reconstruction can be seen in fig. 18.

460 Fig. 19 shows reconstructed brightnesses of laser tracks in the detector vs
461 the laser shot energy, for the distance of 33 km. In the tested energy range
462 of 4–22 mJ, which is below the saturation of the detector, the dependency is
463 linear, showing that EUSO-TA behaves as expected. For the lowest energies
464 of about 2–3 mJ, only a few of the brightest laser events were reconstructed,
465 resulting in a brightness cut on the data. While lowering the threshold of
466 the reconstruction algorithm allowed for the detection of more events, the
467 cut shows the point at which the detector starts to become limited by the

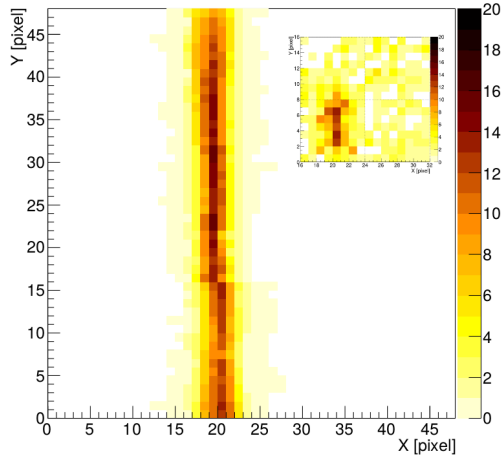


Figure 14: An average of 259 tracks of the CLF laser, for a telescope elevation angle of 10° . The inset shows a part of a single frame containing the laser. The colour scale denotes the uncalibrated detector counts.

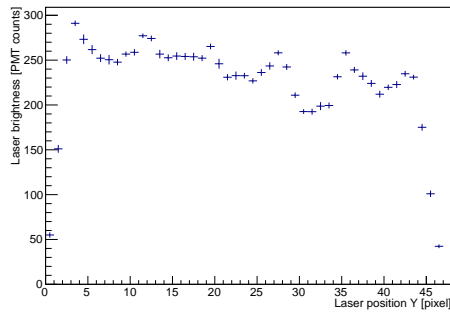


Figure 15: A profile histogram of 259 CLF laser tracks, for telescope elevation angle of 10° . The values show the average of summed counts for laser spots in a specific position on the frame. The brightness is lower for spots falling into space between MAPMTs or outside the PDM.

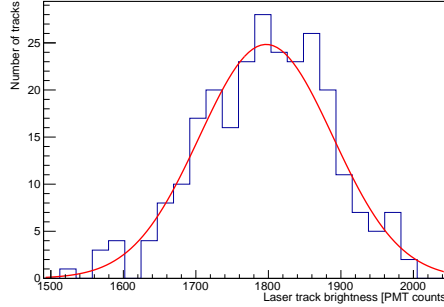


Figure 16: The reconstructed distribution of the integrated number of counts from 259 CLF shots. The standard deviation of the fitted Gaussian function is about 5%, comparable to the overall intrinsic CLF energy dispersion of 6%.

468 background. The detection limit for the laser shots of energies 2–4 mJ implies
 469 an energy threshold for detectable UHECR of energies $10^{19.7}$ – 10^{20} eV [26] at
 470 33 km distance. However, it was also possible to detect a few shots of 1 mJ
 471 energy shot vertically from 33 km distance in the EUSO-TA data.

472 4.5. UHECR

473 To date, 9 UHECR events (fig. 20) have been identified in 130 hours of
 474 UHECR-dedicated observations. The distances of these events from the de-
 475 tector vary between approximately 1 and 9 km, while the energy is between
 476 $10^{17.7}$ – $10^{18.8}$ eV, according to the TAFD reconstruction. The proximity
 477 of the events and the dead time between frames makes 8 events visible in
 478 the detector for a duration of a single frame, and one event for two frames.
 479 EUSO-TA does not usually observe the maximum of the shower, but a late
 480 stage of the shower development, and as such the number of registered pho-
 481 tons corresponds to a shower of lower energy than if the instrument was
 482 optimally pointed towards the shower maximum. Therefore, to estimate the
 483 instrument’s capabilities it was necessary to calculate the equivalent ener-
 484 gies of the events (E_{eq}), corresponding to the reconstructed energy assuming
 485 that EUSO-TA observed the event’s shower maximum. This calculation is
 486 based on the parameters measured by TA for each individual shower. The
 487 corresponding points can be used to form a conservative estimate of the de-
 488 tector’s energy threshold. In a very simplified approach, one can assume that
 489 the minimal number of counts on the focal surface for the cosmic ray to be

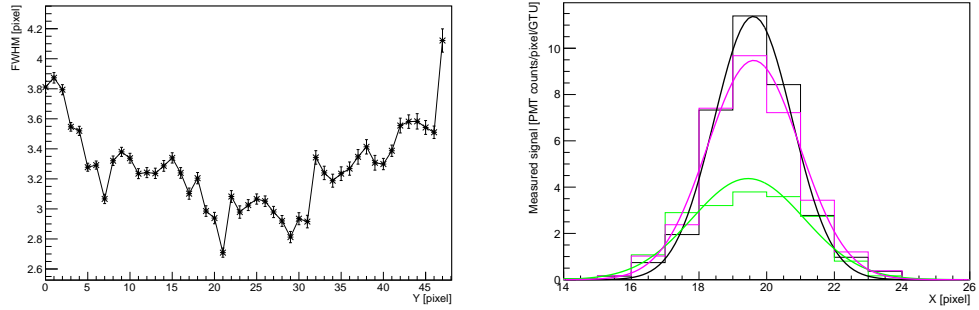


Figure 17: Left: the width of the CLF averaged track in each row (elevation), measured as a FWHM of a fitted Gaussian profile; Right: horizontal cross-sections of the CLF track. Three histograms show cross-sections in Y positions corresponding to the largest, smallest and intermediate widths, with fitted Gaussian profiles.

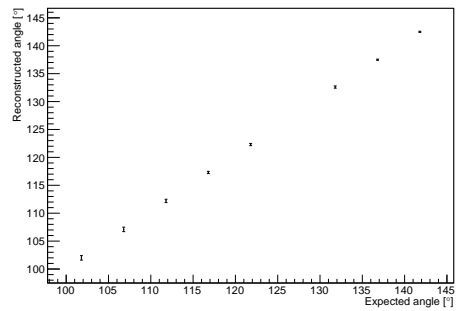


Figure 18: Reconstructed angle vs expected angle for GLS laser pointing sweep. Barely visible error bars show the standard deviation of the distribution of reconstructed angles.

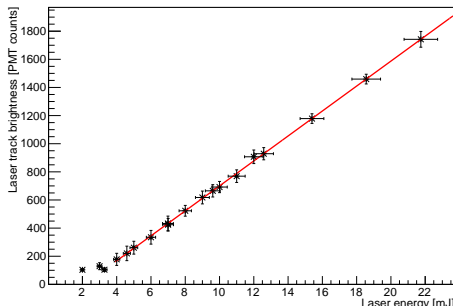


Figure 19: Summed signal of the GLS laser track vs its energy for the distance of 33 km from the detector. The plot sums 2 shooting sessions, altogether encompassing an energy range of 2–22 mJ. Each point was calculated from a few dozens shots. Fitted line shows good linearity of the detector response in the range of 4–22 mJ, while for lower energies only the brightest tracks were reconstructed, enforcing a low brightness cut on the data points.

490 detected is constant, proportional to its energy and reversely proportional to
 491 the square of the distance from the shower axis (R_p). Based on this assump-
 492 tion, $R_p = A \cdot \sqrt{E_{eq}}$ is fit to detected events, where A is a free parameter. It
 493 can be seen that the strong signals of the CLF shots (EAS equivalent energy
 494 of $\sim 10^{19.4}$ eV at a distance of 21 km) and GLS laser shots (EAS equivalent
 495 energy of $\sim 10^{19.7}$ eV and $\sim 10^{20}$ eV at a distance of 33 km) are on the right
 496 side of the curve, i.e. in the detectable region, as expected.

497 Two typical events are shown in fig. 21. It can be seen that re-binning of
 498 the images significantly increases the visibility of the tracks – making EUSO-
 499 TA data more similar to those of ground-based UHECR telescopes, which
 500 have much larger pixel sizes. However, such a pixel size is not suited for space-
 501 based observations, to which EUSO-TA has been tuned. Simulations of the
 502 events made with the “OffLine” package [27] are also presented here. The
 503 shower image can be reproduced to very fine detail, however, some overesti-
 504 mation of the signal in the simulation can be spotted on the residuals shown
 505 in fig. 22 (left). Positive residuals, shown in the picture, align mainly in the
 506 shower area, while negative, which were excluded here for the sake of clarity,
 507 are randomly scattered over the whole field of view. Therefore the higher
 508 UHECR counts in the simulation cannot be attributed solely to statistical
 509 fluctuations. This difference can come both from intrinsic characteristics of

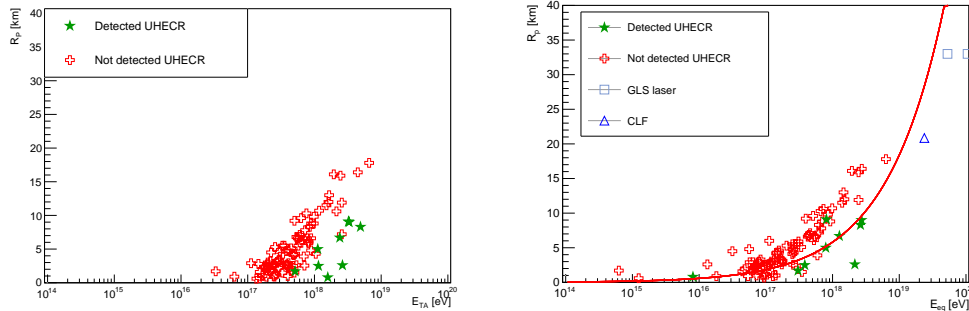


Figure 20: All UHECR detected by TAFD in the EUSO-TA field of view during its operation with non-detected events and laser shots superimposed. The vertical axis shows the distance to the shower axis. Left: the horizontal axis shows the energy of the event as measured by TA. Right: the horizontal axis shows the events equivalent energy (explained in the text). The fit to the detected points, explained in the main text, suggests a conservative estimate of the EUSO-TA detection energy threshold.

510 the model and from uncertainties of shower parameters as measured by TA.
 511 As this problem will be addressed in the future development of the OffLine
 512 package, the detailed analysis of residuals is not presented in this paper.

513 The small pixel size of EUSO-TA decreases the sensitivity but in turn
 514 gives higher spatial resolution compared to most other fluorescence tele-
 515 scopes. This allows for the study of the transversal profile of an EAS, as
 516 shown on fig. 22 (right). The presented shower has a FWHM of 5.27 pixels.

517 In principle EUSO-TA should see only the fraction of UHECR detected by
 518 TAFD which both cross the field of view and are above the energy threshold.
 519 However, with the implementation of the external trigger, data is collected
 520 for each TAFD event. Therefore, an event is considered as detected if a
 521 linear trace is found in the EUSO-TA data and a corresponding event in
 522 TAFD results.

523 Simulations studies carried out in 2011 [13], prior to the installation of
 524 the telescope, predicted the detection of about 15 events in the total data
 525 acquisition time achieved to date. However, that analysis assumed more
 526 optimal EUSO-TA elevation angle of 30° , instead of the most often used $10^\circ -$
 527 15° . Additionally, the analysis assumed a lower background light level than
 528 what was measured. In 2016, further simulations were performed, using the
 529 updated detector parameters [28], resulting in 8 predicted events, consistent

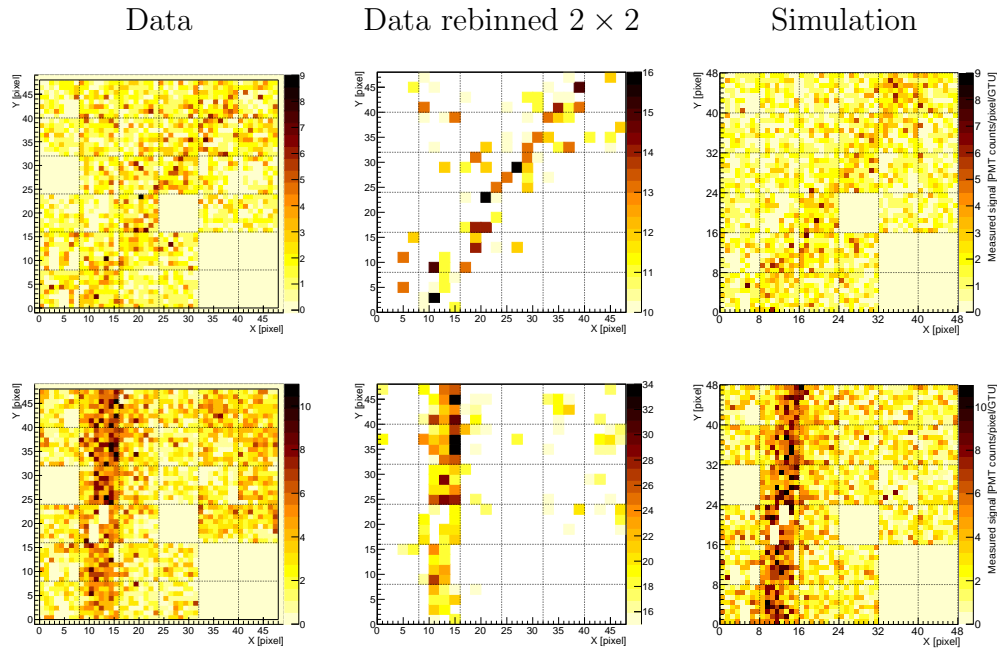


Figure 21: Two out of the 9 UHECR observed by EUSO-TA. The left plot shows the real data in photoelectron counts, in the centre 2×2 rebinning of the data is shown and in the right plot the simulation made with the OffLine package. The top panels are for an event of energy of 10^{18} eV, impact parameter 2.5 km with respect to the telescope, zenith angle of the axis of 35° and azimuth angle of 7° . The bottom panels correspond to an energy of $10^{18.4}$ eV, impact parameter 2.6 km, zenith angle of the axis of 8° and azimuth angle of 82° .

530 with the 9 UHECR observed to date.

531 These first UHECR events registered with EUSO technology allowed for
 532 an important improvement and optimisation of the reconstruction and simu-
 533 lation software. However, the EAS parameters had to be derived from TAFD
 534 which, thanks to its larger field of view and higher time-resolution, could see
 535 the full shower development. Investigation of the parameters of the UHECR
 536 events which occurred inside the EUSO-TA field of view during its operation,
 537 starts to reveal the detection capabilities of the detector.

538

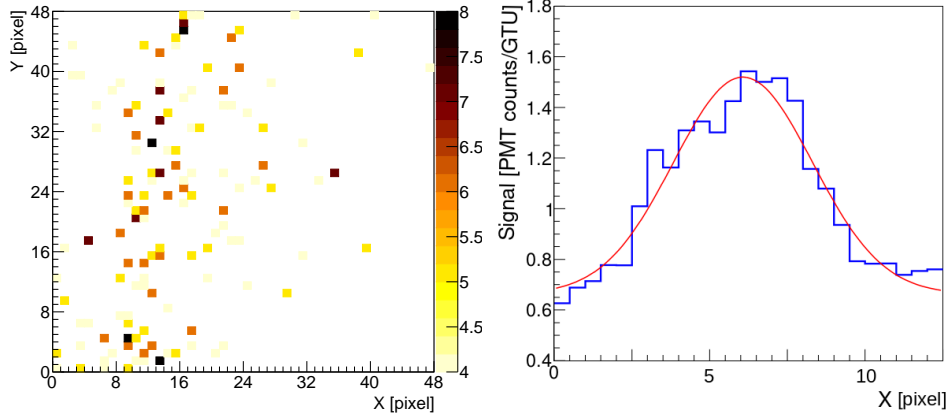


Figure 22: Left: Residues of the data subtracted from simulation for the second UHECR shown in fig. 21. The colour scale, in detector counts, is set to emphasise the part including the shower; Right: transversal profile of the same UHECR with subpixel resolution, corrected for the EAS non-vertical axis (the correction causes shift of the maximum compared to the original shower axis and X axis crossing point). The Gaussian fit gives FWHM of 5.27 pixels.

539 5. EUSO-TA future plans

540 EUSO-TA provides an excellent opportunity to test technology for ex-
 541 isting and future experiments within the EUSO framework, as it allows for
 542 stable field observations for extended time periods. However, the observa-
 543 tion time could be significantly increased if remote automatic operation of
 544 the instrument was implemented. This would allow for the collection of data
 545 continuously over the year in all possible observational periods. This task
 546 will require introduction of some additional mechanical and control devices,
 547 as well as a non-remote automatic working test period.

548 The sensitivity of the experiment will be enhanced with an upgrade of
 549 the EC-ASIC boards to the new version incorporating SPACIROC3 ASIC,
 550 which has ~ 5 ns single pulse resolution instead of the current 30 ns. This
 551 parameter is important for nearby showers, which cross a single pixel in
 552 short timescales. Higher single pulse resolution decreases a chance of several
 553 photons from such an event falling into a single time bin and therefore being
 554 lost. The tests with EUSO-SPB in Utah show about a factor of 2 higher signal
 555 for CLF tracks, which may be attributed mainly to the use of SPACIROC3.

556 The efficiency change should be much higher for close tracks, where the time
557 spent in a single pixel is much shorter.

558 The experiment will also be upgraded with advanced self-triggering capa-
559 bilities. This will be achieved by replacing the current PDM data processing
560 board with a new board based on system-on chip - Zynq XC7Z030 FPGA,
561 recently developed by XILINX, which has more memory and resources. It
562 allows the implementation of data read-out on three timescales, similar to
563 the readout designed for the Mini-EUSO mission. This μs timescale readout
564 is self-triggered, dedicated to UHECR observations. Integrated packets form-
565 ing 320 ms frames would be passed to second level trigger, dedicated mainly
566 to atmospheric phenomena. Finally, ms scale frames integrated to 5.24 s ex-
567 posures would be stored as a “movie” for analysis of slow phenomena, such
568 as strangelets and meteors, detectable with offline event search algorithms.

569 6. Conclusion

570 EUSO-TA demonstrates the performance of a new technology for the ob-
571 servation of cosmic rays, based on using Fresnel lenses and multi-anode pho-
572 tomultipliers. The detector has registered, using TAFD triggers, 9 UHECR
573 during its five observational campaigns, proving that use of Fresnel lenses and
574 multi-anode photomultipliers works well for this purpose. The response of
575 the detector was tested using UV laser shots mimicking extensive air showers.
576 Additionally, a number of “slow” events such as stars, meteors and airplanes
577 has been observed allowing for an extension of the scientific objectives.

578 The main goal of EUSO-TA, was to test the capabilities and stability of
579 the hardware. It proved an invaluable testbench for the modifications applied
580 in the EUSO-SPB and Mini-EUSO detectors.

581 From the 9 registered UHECR an idea of EUSO-TA sensitivity starts to
582 emerge, which is found to be within expectations, especially for one of the
583 first prototypes employing a new technology. Moreover, if the exposure time
584 was reduced from the value of $2.5 \mu\text{s}$ optimised for space-based measurements
585 to the 100 ns used in TAFD as optimised for ground-based measurements,
586 the signal to noise ratio would increase significantly. A similar effect will be
587 achieved through the application of planned hardware upgrades in the future.

588 Results described in this article allowed us to evaluate the performance
589 of an optical system composed of two Fresnel lenses, which behaved accord-
590 ing to predictions. Fresnel-based optics have the advantage of wide field of
591 view, simple design and reduced weight compared to mirror based systems.

592 However, the disadvantages include the increased point spread function (com-
593 pared to mirrors), chromatic aberration (which can be offset by diffractive
594 lenses) and lower optical transmission due to several refractions. The advan-
595 tages of one design over another in space-based systems depends strongly on
596 the mission profile (rocket accommodation, satellite or space station, etc.).

597 A challenging future goal is keeping EUSO-TA up to date with develop-
598 ments of the other experiments in the EUSO framework. Two detectors –
599 the already launched EUSO-SPB and the prepared Mini-EUSO – use a new
600 version of EC-ASIC boards equipped with SPACIROC 3 ASICs, resulting
601 in significantly higher dynamic range and signal to noise ratio. Mini-EUSO
602 also replaces a PDM, CCB and Clock boards with the PDM data processing
603 board allowing for the efficient and parallelised performance of more com-
604 putationally demanding tasks. Introducing these elements to EUSO-TA is a
605 necessary step to increase its performance and keep compatibility with other
606 missions. In the near future an upgrade and automatisisation of the telescope
607 is planned to increase its sensitivity and duty cycle. Also, it is hoped to
608 include an additional middle diffractive Fresnel lens to reduce the PSF and
609 thus increase the signal to noise ratio. Finally, EUSO-TA will be used as a
610 testbench for the development of multi-PDM observations and readout.

611 **Acknowledgments**

612 This work was partially supported by Basic Science Interdisciplinary Re-
613 search Projects of RIKEN and JSPS KAKENHI Grant (22340063, 23340081,
614 and 24244042), by the Italian Ministry of Foreign Affairs and International
615 Cooperation, by the Italian Space Agency through the ASI INFN agree-
616 ment n. 2017-8-H.0, by NASA award 11-APRA-0058 in the USA, by the
617 Deutsches Zentrum für Luft- und Raumfahrt, by the French space agency
618 CNES, the Helmholtz Alliance for Astroparticle Physics funded by the Ini-
619 tiative and Networking Fund of the Helmholtz Association (Germany), by
620 Slovak Academy of Sciences MVTS JEM-EUSO, by National Science Cen-
621 tre in Poland grant (2015/19/N/ST9/03708), by Mexican funding agencies
622 PAPIIT-UNAM, CONACyT and the Mexican Space Agency (AEM), as well
623 as VEGA grant agency project 2/0132/17, and by State Space Corpora-
624 tion ROSCOSMOS and Russian Foundation for Basic Research (grant 16-
625 29-13065). We are grateful to the Telescope Array collaboration for allowing
626 us to use the TA site and its facilities, and for all their help.

627 We dedicate this article to Yoshiya Kawasaki and Jacek Karczmarczyk,
628 who passed away in 2016.

629 **References**

- 630 [1] Y. Takahashi, J.-E. Collaboration, et al., The JEM-EUSO Mission, *New*
631 *Journal of Physics* 11 (6) (2009) 065009.
- 632 [2] L. Porter, J. Earnshaw, E. Tielsch-Cassel, J. Ahlstrom, K. Greisen, A
633 space-time detector for cosmic ray showers, *Nuclear Instruments and*
634 *Methods* 87 (1) (1970) 87 – 92.
- 635 [3] J. Adams, S. Ahmad, J.-N. Albert, D. Allard, L. Anchordoqui, V. An-
636 dreev, A. Anzalone, Y. Arai, K. Asano, M. A. Pernas, et al., The EUSO-
637 Balloon pathfinder, *Experimental Astronomy* 40 (1) (2015) 281–299.
- 638 [4] M. Ricci, M. Casolino, P. Klimov, Mini-EUSO: a pathfinder for JEM-
639 EUSO to measure Earths UV background from the ISS, *Proceedings of*
640 *Science. PoS (ICRC2015)* 599.
- 641 [5] B. A. Khrenov, V. V. Alexandrov, D. I. Bugrov, G. K. Garipov, N. N.
642 Kalmykov, M. I. Panasyuk, S. A. Sharakin, A. A. Silaev, I. V. Yashin,
643 V. M. Grebenyuk, D. V. Naumov, A. G. Olshevsky, B. M. Sabirov, R. N.
644 Semenov, M. Slunechka, I. I. Skryl, L. G. Tkatchev, O. A. Saprykin, V. S.
645 Syromyatnikov, V. E. Bitkin, S. A. Eremin, A. I. Matyushkin, F. F.
646 Urmantsev, V. Abrashin, V. Koval, Y. Arakcheev, A. Cordero, O. Mar-
647 tinez, E. Morena, C. Robledo, H. Salazar, L. Villasenor, A. Zepeda,
648 I. Park, M. Shonsky, J. Zicha, KLYPVE/TUS space experiments for
649 study of ultrahigh-energy cosmic rays, *Physics of Atomic Nuclei* 67 (11)
650 (2004) 2058–2061. doi:10.1134/1.1825529.
651 URL <https://doi.org/10.1134/1.1825529>
- 652 [6] P. Klimov, C. M., Status of the KLYPVE-EUSO detector for EECR
653 study on board the ISS, *Proc. of the ICRC2017*.
- 654 [7] Y. Tameda, et al., Telescope Array Experiment, *Nuclear Physics B-*
655 *Proceedings Supplements* 196 (2009) 74–79.

- 656 [8] H. Prieto-Alfonso, L. del Peral, M. Casolino, K. Tsuno, T. Ebisuzaki,
657 M. Frías, J.-E. Collaboration, Multi Anode Photomultiplier Tube Re-
658 liability Assessment for the JEM-EUSO Space Mission, arXiv preprint
659 arXiv:1501.05908.
- 660 [9] H. Miyamoto, K. Yoshida, F. Kajino, S. Ahmad, P. Barrillon, S. Blin-
661 Bondil, S. Dagoret-Campagne, C. de la Taille, F. Dulucq, P. Gorodetzky,
662 et al., Performance of the SPACIROC front-end ASIC for JEM-EUSO,
663 The JEM-EUSO Mission: Contributions to the ICRC 2013 (2013) 103.
- 664 [10] J. Bayer, G. Distratis, D. Gottschall, A. Santangelo, C. Tenzer,
665 M. Bertaina, M. Casolino, G. Osteria, J.-E. Collaboration, Second level
666 trigger and Cluster Control Board for the JEM-EUSO mission, in: Pro-
667 ceedings of 33rd International Cosmic Ray Conference, Rio de Janeiro,
668 Brazil, 2013, pp. 99–102.
- 669 [11] F. Kajino, M. Casolino, T. Ebisuzaki, J. Adams, P. Ballmoos,
670 M. Bertaina, M. Christl, S. Dagoret, C. De La Taille, M. Fukushima,
671 et al., The JEM-EUSO Instruments, in: 33rd International Cosmic Ray
672 Conference (ICRC2013), 2013.
- 673 [12] V. Scotti and G. Osteria on behalf of the JEM-EUSO Collaboration,
674 The Data Processor of the JEM-EUSO pathfinders, in: Astroparticle,
675 Particle, Space Physics and Detectors for Physics Applications, pp. 120–
676 124.
- 677 [13] L. W. Piotrowski, M. Casolino, L. Conti, T. Ebisuzaki, C. Fornaro,
678 Y. Kawasaki, Y. Hachisu, H. Ohmori, C. De Santis, K. Shinozaki, et al.,
679 On-line and off-line data analysis for the EUSO-TA experiment, Nuclear
680 Instruments and Methods in Physics Research Section A: Accelerators,
681 Spectrometers, Detectors and Associated Equipment 773 (2015) 164–
682 171.
- 683 [14] T. Fujii, M. Malacari, M. Bertaina, M. Casolino, B. Dawson, P. Horvath,
684 M. Hrabovsky, J. Jiang, D. Mandat, A. Matalon, et al., Detection of
685 ultra-high energy cosmic ray showers with a single-pixel fluorescence
686 telescope, *Astroparticle Physics* 74 (2016) 64–72.
- 687 [15] J. Adams, E. Kuznetsov, J. Watts, S. Csorna, M. Rodencal, L. W. Pi-
688 otrowski, M. Mustafa, Calibration of the EUSO-TA Prototype Instru-
689 ment, *PoS* (2015) 582.

- 690 [16] H. Johnson, W. Morgan, Fundamental stellar photometry for standards
691 of spectral type on the revised system of the Yerkes spectral atlas, *The*
692 *Astrophysical Journal* 117 (1953) 313.
- 693 [17] M. A. Perryman, L. Lindegren, J. Kovalevsky, E. Hoeg, U. Bastian,
694 P. Bernacca, M. Cr ez e, F. Donati, M. Grenon, M. Grewing, et al., *The*
695 *HIPPARCOS catalogue*, *Astronomy and Astrophysics* 323 (1997) L49–
696 L52.
- 697 [18] L. Piotrowski, T. Batsch, H. Czyrkowski, M. Cwiok, R. Dabrowski,
698 G. Kasprowicz, A. Majcher, A. Majczyna, K. Malek, L. Mankiewicz,
699 et al., PSF modelling for very wide-field CCD astronomy, *Astronomy &*
700 *Astrophysics* 551 (2013) A119.
- 701 [19] Z. Plebaniak, J. Szabelski, T. Wibig, L. Piotrowski, et al., Point Spread
702 Function of EUSO-TA detector, in: *Proceedings of 35th International*
703 *Cosmic Ray Conference*, Busan.
- 704 [20] J. Abraham, P. Abreu, M. Aglietta, C. Aguirre, E. Ahn, D. Allard,
705 I. Allekotte, J. Allen, P. Allison, J. Alvarez-Muniz, et al., The fluores-
706 cence detector of the Pierre Auger Observatory, *Nuclear Instruments*
707 *and Methods in Physics Research Section A: Accelerators, Spectrometers,*
708 *Detectors and Associated Equipment* 620 (2) (2010) 227–251.
- 709 [21] M. Hayashi, Y. Tameda, T. Tomida, Y. Tsunesada, T. Seki, Y. Saito,
710 Development of a UAV-mounted Light Source for Fluorescence Detector
711 Calibration of the Telescope Array Experiment, in: *Proceedings*
712 *of 2016 International Conference on Ultra-High Energy Cosmic Rays*
713 *(UHECR2016)*, 2018, p. 011036.
- 714 [22] T. Ebisuzaki, M. N. Quinn, S. Wada, L. W. Piotrowski, Y. Takizawa,
715 M. Casolino, M. E. Bertaina, P. Gorodetzky, E. Parizot, T. Tajima,
716 et al., Demonstration designs for the remediation of space debris from
717 the International Space Station, *Acta Astronautica* 112 (2015) 102–113.
- 718 [23] J. Adams, S. Ahmad, J.-N. Albert, D. Allard, L. Anchordoqui, V. An-
719 dreev, A. Anzalone, Y. Arai, K. Asano, M. A. Pernas, et al., *JEM-*
720 *EUSO: Meteor and nuclearite observations*, *Experimental Astronomy*
721 40 (1) (2015) 253–279.

- 722 [24] Y. Takahashi, K. Yamazaki, D. Ikeda, H. Sagawa, H. Tokuno,
723 K. Hayashi, M. Fukushima, S. Ogio, S. Udo, T. Fujii, et al., Central
724 laser facility analysis at the Telescope Array experiment, in: AIP Con-
725 ference Proceedings, Vol. 1367, AIP, 2011, pp. 157–160.
- 726 [25] P. Hunt , R. Bachman, J. Eser, M. Mantz, L. Wiencke, C. Baron, C.
727 Bigler, D. Bruzgo, M. Burg, A. Cain, A. Cummings, A. Evans, W. Finch,
728 J. Fruit, T. Gallmeyer, C. Geier, J. Gossman, D. Hirsch, R. Hanley, A.
729 Osieczanek, I. Smith, and T. Wills, for the JEM-EUSO Collaboration,
730 The JEM-EUSO Global Light System Laser Station Prototype, PoS
731 (ICRC2015) 626.
- 732 [26] A. L. Cummings, Field Testing for EUSO-SPB: Logistics and First Re-
733 sults, Ph.D. thesis, Colorado School of Mines. Arthur Lakes Library.
- 734 [27] T. Paul, M. Bertaina, F. Bisconti, J. Eser, G. Figueiredo, M. Fouka,
735 F. Guarino, L. Del Peral, Z. Sahnoun, et al., New simulation and recon-
736 struction software for the EUSO pathfinders, with example applications,
737 Proc. of the ICRC2017.
- 738 [28] F. Bisconti, et al., Simulation study of the detected and expected events
739 for the EUSO-TA fluorescence detector, in: Proceedings of 35th Inter-
740 national Cosmic Ray Conference, Busan, Korea, 2017.